Japanese Journal of Applied Physics

PROGRESS REVIEW

Polarized terahertz electromagnetic-wave radiation from cuprate superconductor Bi2212 mesa structures

To cite this article: Asem Elarabi *et al* 2024 *Jpn. J. Appl. Phys.* **63** 020801

Japanese Journal of Applied Physics **63**, 020801 (2024) **PROGRESS REVIEW**
https://doi.org/**10.35848/1347-4065/ad0cdd**

Polarized terahertz electromagnetic-wave radiation from cuprate superconductor Bi2212 mesa structures

Asem Elarabi[1], Yoshito Saito[2,3], Hidehiro Asai[4], Ryota Kobayashi[1], Ken Hayama[1], Keiichiro Maeda[1], Shuma Fujita[1], Yusuke Yoshioka[1], Yoshihiko Takano[2,3], Manabu Tsujimoto[5], and Itsuhiro Kakeya[1*]

[1]*Department of Electronic Science and Engineering, Kyoto University, Kyotodaigaku Katsura, Nishikyo, Kyoto 615-8510, Japan*
[2]*International Center for Materials Nanoarchitectonics (MANA), National Institute for Materials Science, Tsukuba, Ibaraki 305-0047, Japan*
[3]*Graduate School of Pure and Applied Sciences, University of Tsukuba, 1-1-1 Tennodai, Tsukuba, Ibaraki 305-8577, Japan*
[4]*Semiconductor Frontier Research Center, National Institute of Advanced Industrial Science and Technology (AIST), Central 2, 1-1-1 Umezono, Tsukuba, Ibaraki 305-8568, Japan*
[5]*Global Research and Development Center for Business by Quantum-AI Technology (G-QuAT), National Institute of Advanced Industrial Science and Technology (AIST), Central 2, 1-1-1 Umezono, Tsukuba, Ibaraki 305-8568, Japan*

[*]E-mail: kakeya@kuee.kyoto-u.ac.jp

Received July 31, 2023; revised November 2, 2023; accepted November 15, 2023; published online January 4, 2024

Polarized terahertz (THz) sources are important components in THz technologies. This paper highlights and discusses recent progress and measurement methods in the monolithic generation of polarized THz radiation using intrinsic Josephson junction oscillators made of high-T_c superconductors. The polarized radiation is generated from three mesa designs: truncated-edge square, notched cylindrical, and rectangular mesa structures. The polarization control depends on the excitation of two orthogonal TM modes in these mesas, comprising stacked intrinsic Josephson junctions in single crystalline $Bi_2Sr_2CaCu_2O_{8+\delta}$. This method maintains a high output intensity and low axial ratios while avoiding the signal loss associated with external polarimetric modulators prevalent in the THz frequency range. Moreover, it demonstrates the manipulation of terahertz wave helicity by adjusting the current injection position, with experiments substantiating the device's capability to switch between left-handed and right-handed elliptical polarization at designated frequencies. © 2024 The Japan Society of Applied Physics

1. Introduction

Electromagnetic (EM) wave sources operating in the terahertz (THz) frequency range have recently attracted increasing interest.[1)] Their potential applications span a wide range of scientific and technological domains, from materials science and astronomy to ultra-high-speed communications,[2,3)] security systems,[4)] and biomedical research.[5,6)] To meet the diverse needs of these applications, a variety of EM wave sources have been developed. Among these sources, semiconductor-based devices such as quantum cascade lasers[7)] and resonant tunneling diode-based oscillators[8)] are often cited as highly promising candidates. Superconducting devices made from $Bi_2Sr_2CaCu_2O_{8+\delta}$ (Bi2212), proved to be a strong candidate for reliable THz sources.[9–14)]

In the case of highly anisotropic superconductors like such as Bi2212, it is possible to study the properties of individual intrinsic Josephson junctions (IJJs), revealing a rich array of superconducting phenomena. These include the *d*-wave nodal superconducting gap, the first-order vortex lattice melting transition, macroscopic quantum tunneling at low temperatures, and EM wave emissions resulting from the synchronous oscillations of numerous IJJs.[15)] Terahertz EM wave emissions from IJJ stacks in Bi2212 single crystals were initially demonstrated in 2007 and were found to be the result of synchronized Josephson plasma waves excited in IJJs according to the ac Josephson effect.[9)] We refer to such devices as Josephson plasma emitters (JPEs).[11)] To make JPEs practical for telecommunication and imaging applications, their output power must exceed 1 mW, which is the sensitivity limit of state-of-the-art terahertz cameras. Recent advances in JPE research have focused on improving frequency tunability,[16–18)] operating temperature,[19–21)] and fabrication techniques.[22,23)] Although the radiation power of the JPEs still lags behind other THz sources, recent studies have shown promise in improving the output power through synchronized emissions from coupled devices. The maximum output power of a JPE attained by driving three mesa structures on a crystal is 0.61 mW, which is approximately 32 times the individual emission power.[24)]

Efforts to improve radiation efficiency and discover new functionalities for JPEs are of great significance in the field of superconducting electronics. Efficient HF radiation in Josephson junctions is achieved through phase-locking to an external resonance condition. Various techniques have been studied to achieve phase-locking in one and two-dimensional JJs arrays, such as by coupling the array to an external LCR resonator, or using a common ground plane, and locking them by cavity resonance as explained in these references.[25,26)] The power emitted by such an array is directly proportional to N^2, where N is the number of contributing junctions. It has been confirmed that, based on its current–voltage ($I-V$) characteristics, the layered structure of Bi2212 functions as a series-connected one-dimensional array of Josephson junctions, leading to the term IJJs.[27–29)] By using Bi2212 IJJs, it was theoretically foreseen[30–32)] and experimentally realized[9)] that high radiation power can be achieved through phase-locked synchronized Josephson plasma waves in resonance with the cavity.

The ability to manipulate radiation properties like directionality and polarization in JPEs is a subject of particular interest, as it expands the range of potential applications for these devices. Theoretical models have predicted that emissions from rectangular mesas should exhibit linear polarization:[33,34)] a prediction that has been corroborated by experimental studies utilizing radiation patterns.[35)] Additionally, it has been theoretically shown that polarization in JPEs can be modified through induction of thermal inhomogeneity on the surface of the device.[36,37)] These works imply that polarization is an important measure including rich variery of physics not only electromagnetism but also superconductivity and the patch anttena theory

developped in microwave range[38] is applicable for controling terahertz radiation from JPE. In this paper, we discuss a subset of experiments related to this subject that we have conducted. It is pertinent to note that some of the findings and discussions presented in this review have their origins in the author's published thesis and other publications.[39–48]

2. Polarization in the THz range

Polarization control in the THz region has been a highly targeted field for the past 30 years. Achieving such control could pave the way for numerous practical applications, ranging from telecommunications and imaging to spectroscopy. Although polarization control of pulsed THz radiation has been well documented in various studies using methods such as liquid crystal cells,[49] laser pulse combinations,[50,51] dual-color lasers,[52,53] and femtosecond pulse modulators,[54,55] it is generally more challenging to control polarization in continuous-wave devices. Conventionally, circularly polarized radiation has been achieved in laboratories using polarization converters or phase-retarders. While this is straightforward at optical frequencies using birefringence or chiral effects of anisotropic materials, such as quarter-wave plates, achieving the requisite phase delay is more challenging at submillimeter wavelengths.[56] Various alternative methods have been explored, including frequency selective surfaces,[57–59] metasurfaces,[59–62] waveguides,[63] and artificially periodic metamaterials.[64–67]

It has been previously demonstrated that the polarization state of spin-polarized lasers and LEDs can be tuned by an applied external magnetic field,[68,69] achieving a degree of circular polarization (DOCP) of up to 50%. A more practical approach for field applications would be to integrate polarization control into a single, unified structure, commonly referred to as monolithic polarization control. This would minimize radiation loss and simplify the overall system. In support of this concept, various studies have developed monolithic circularly polarized terahertz sources. These sources typically use quantum cascade lasers (QCLs) as a radiation source and are covered with "fishbone" surface gratings composed of orthogonally oriented aperture antennas.[70,71] A high DOCP ($\approx 98\%$) was observed using these types of sources.[70] Liang et al. showed that THz radiation could be continuously tuned from linear to circular polarization (CP) by electronically and monolithically integrating in-plane metasurfaces with two phase-locked semiconductor-based THz QCLs.[72] Furthermore, a device with a switchable polarization state was also demonstrated.[73]

In the microwave region, polarization control finds applications in diverse fields including telecommunications, radar, and navigation systems. There are two primary methods for achieving polarization control in this frequency range: the use of antennas and waveguides. The antenna approach becomes particularly relevant when exploring THz radiation generated by IJJs. The mesa structure in IJJs closely resembles a patch antenna, especially since its radiation is governed by resonance conditions.[38,74,75] This similarity enables the application of antenna theory for the design and understanding of IJJ-based devices to control radiation properties,[40,41,76–78] a topic that will be explored more later in this review.

3. Polarization of EM waves and Stokes formalism

In the case where the polarization is *linear*, the electric field oscillates in one direction. If the electric field rotates at a constant rate in the direction of propagation, then the polarization is considered elliptical or circular, depending on the rotation properties. The rotation could be rotating to the right (viewing from the detector to the emitter, termed left-hand polarization) or rotating to the left (termed Right-Hand Polarization). The pioneering studies by Fresnel and Arago showed that an EM wave consists of two orthogonally linearly polarized electric field components:[79–82]

$$E_x(z,\,t) = E_{0x}\,\cos[\omega t - kz + \delta_x], \tag{1}$$

$$E_y(z,\,t) = E_{0y}\,\cos[\omega t - kz + \delta_y], \tag{2}$$

where, E_{0x} and E_{0y} represent the peak amplitudes, $\omega t - kz$ acts as the electric field propagator, z denotes the direction of propagation, t is indicative of time, while δ_x and δ_y symbolize the phases at the x and y axis, both of which are perpendicular to the direction of propagation. If one were to map the trajectory of this polarized electric field over time and space, the result would be an elliptical shape. This ellipse, known as

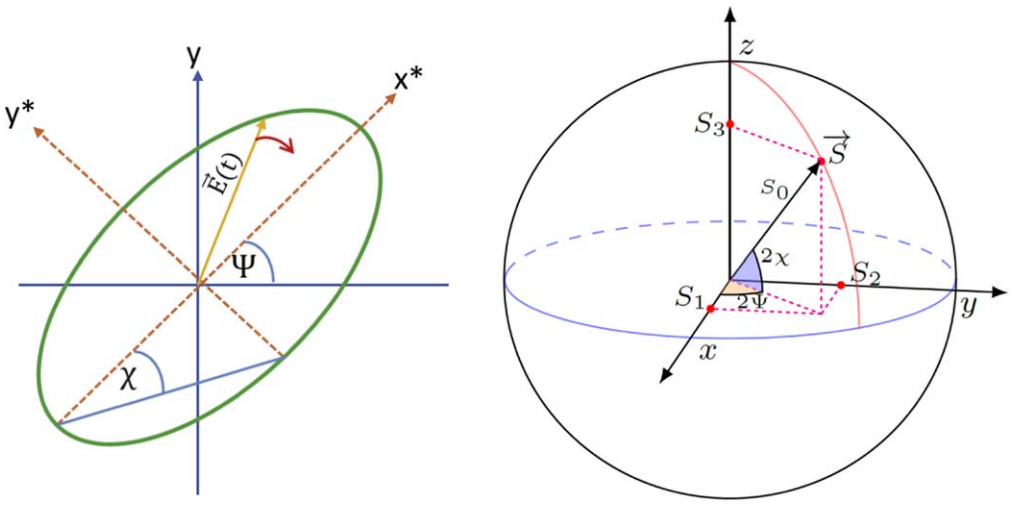

Fig. 1. (Lefft) Polarization ellipse. (Right) Poincaré sphere represents a visualization method to Stokes parameters, pointing to a point on the sphere surface (red dot). The length of the Stokes vector ($\vec{S}$) corresponds to the total intensity (I_{total} or S_0), while the remaining Stokes parameters (S_1, S_2, S_3) are denoted by their projections onto the x, y, and z axis, respectively. Reproduced from Ref. 39 with permission of Asem Elarabi.

the *polarization ellipse*, is depicted in Fig. 1. The nature of this ellipse can be further detailed by:[82)]

$$\frac{E_x^2(t)}{E_{0x}^2} + \frac{E_y^2(t)}{E_{0y}^2} - \frac{2E_x(t)E_y(t)}{E_{0x}E_{0y}}\cos\delta = \sin^2\delta. \tag{3}$$

The polarization state can be characterized using the geometric parameters of the polarization ellipse. This involves the use of the AR, which represents the ratio of the ellipse's major axis to its minor axis (a/b), or its inverse, known as the ellipticity (b/a). The orientation angle (Ψ) is defined as the angle between the ellipse's major axis and the x-axis. The ellipticity angle (χ), indicative of the polarization ellipse's "roundness" or "stretch", is also depicted in the figure. Both Ψ and χ can be mathematically described according to the following equations:[38,82)]

$$\tan 2\Psi = \frac{2E_{0x}E_{0y}\cos\delta}{E_{0x}^2E_{0y}^2}, \tag{4}$$

$$\sin 2\chi = \frac{2E_{0x}E_{0y}\sin\delta}{E_{0x}^2 + E_{0y}^2}, \tag{5}$$

$$AR = \frac{\text{majoraxis}}{\text{minoraxis}} = \frac{a}{b} \quad 1 \leqslant AR \leqslant \infty, \tag{6}$$

where

$$b = \sqrt{\frac{1}{2}(E_{0x}^2 + E_{0y}^2 + \sqrt{E_{0x}^4 + E_{0y}^4 + 2E_{0x}^2E_{0y}^2\cos 2\delta})}, \tag{7}$$

and

$$a = \sqrt{\frac{1}{2}(E_{0x}^2 + E_{0y}^2 - \sqrt{E_{0x}^4 + E_{0y}^4 + 2E_{0x}^2E_{0y}^2\cos 2\delta})}. \tag{8}$$

In order to provide a more comprehensive mathematical description of the polarization state, four parameters are typically used. These parameters, known as Stokes polarization parameters (SPPs),[83)] are useful and quantifiable metrics capable of accurately characterizing fully polarized, partially polarized, and nonpolarized EM waves. They can be defined mathematically as:

$$S_0 = E_{0x}^2 + E_{0y}^2, \tag{9}$$

$$S_1 = E_{0x}^2 - E_{0y}^2, \tag{10}$$

$$S_2 = 2E_{0x}E_{0y}\cos\delta, \tag{11}$$

$$S_3 = 2E_{0x}E_{0y}\sin\delta. \tag{12}$$

The first parameter S_0 represents the total intensity of the EM wave. The second parameter S_1 measures the value of the horizontal and vertical linear polarization. S_2 characterizes the linear polarization at angles of 45° or −45°. Lastly, S_3 indicates the rotation direction of the EM wave, specifying whether it is right-hand CP (RHCP) or left-hand CP (LHCP). Figure 2 provides a schematic representation of the states of polarization of EM waves with respect to their defining SPPs. To gauge the portion of unpolarized EM waves within the total measured radiation, an insightful expression known as the degree of polarization (DOP) can be utilized. It is defined as the ratio of the intensity of polarized waves to the total measured intensity, and can be expressed as follows:

$$\begin{aligned} \text{DOP} &= \sqrt{(S_1^2 + S_2^2 + S_3^2)}/S_0, \\ 0 \quad &\leqslant \quad \text{DOP} \leqslant 1. \end{aligned} \tag{13}$$

If DOP = 0, this signifies that the entire measured radiation is unpolarized. On the contrary, if DOP = 1, it denotes that all measured radiation is polarized. When $0 < \text{DOP} < 1$, it implies the presence of partially polarized radiation.

An additional method to visualize the polarization state is through the use of a Poincaré sphere [Fig. 1]. The SPPs are depicted as a vector originating from the center point (0,0,0) and extending to the sphere's surface. Figure 2 further illustrates the states of polarization as represented by the Poincaré sphere for different SPPs.

4. Experimental details

4.1. Samples fabrication and measurement setups

High-quality single crystals of Bi2212 are prepared in-lab using the traveling solvent floating zone technique. The mesa shape is then fabricated using photolithography and argon ion milling.

Figure 3 shows the electrical wiring block diagram. THz emission is detected using a lock-in amplifier (Sanford Research System SR850), an optical chopper and a Si bolometer, as shown in Fig. 4. All measurements are made in a nitrogen-purged box. A thermally controlled He-flow cryostat equipped with an optical window was used. For the frequency spectra measurements, a Martin–Puplett type FTIR spectrometer[84)] was employed for the truncated-edge square (TES) and rectangular mesa, while a split lamellar mirror spectrometer was used for the notched-side cylindrical mesa type.[85,86)]

4.2. Polarization measurements

The polarization of a radiated EM wave is described by the curve traced by the momentary electric field radiated by the antenna in a plane perpendicular to the radial direction.[38)] This projection takes on an elliptical shape.

The polarization of sources is often characterized by the AR, the tilt of the polarization ellipse (Ψ), and the rotation direction or helicity. In practice, it is challenging to achieve a radiation source that has a constant polarization state in all directions. Therefore, the polarization is typically measured at the point where the source is intended to be used. A comprehensive characterization of polarization should include not only AR and Ψ but also the direction of rotation (either right-handed or left-handed rotation). It should be noted that some of the results presented in this review were obtained using the method known as the *polarization-pattern method*. Although this method can determine the AR and tilt angle of the polarization ellipse, it does not provide information on the rotation direction.

4.2.1. AR measurement with a wire-grid polarizer. To measure AR and Ψ, the polarization-pattern method calls for the use of a linearly polarized receiver as a probing device. In some studies, a combination of a silicon bolometer with a wire-grid polarizer (WGP) is utilized for this purpose. As depicted in Fig. 5(a), the THz emission source is mounted inside a cryostat. The angle of the WGP is controlled using a stage controller and a motor. As the WGP rotates in the beam path [Fig. 5(a)], the change in intensity is recorded in relation to the angle of the polarizer. In cases of linear polarization,

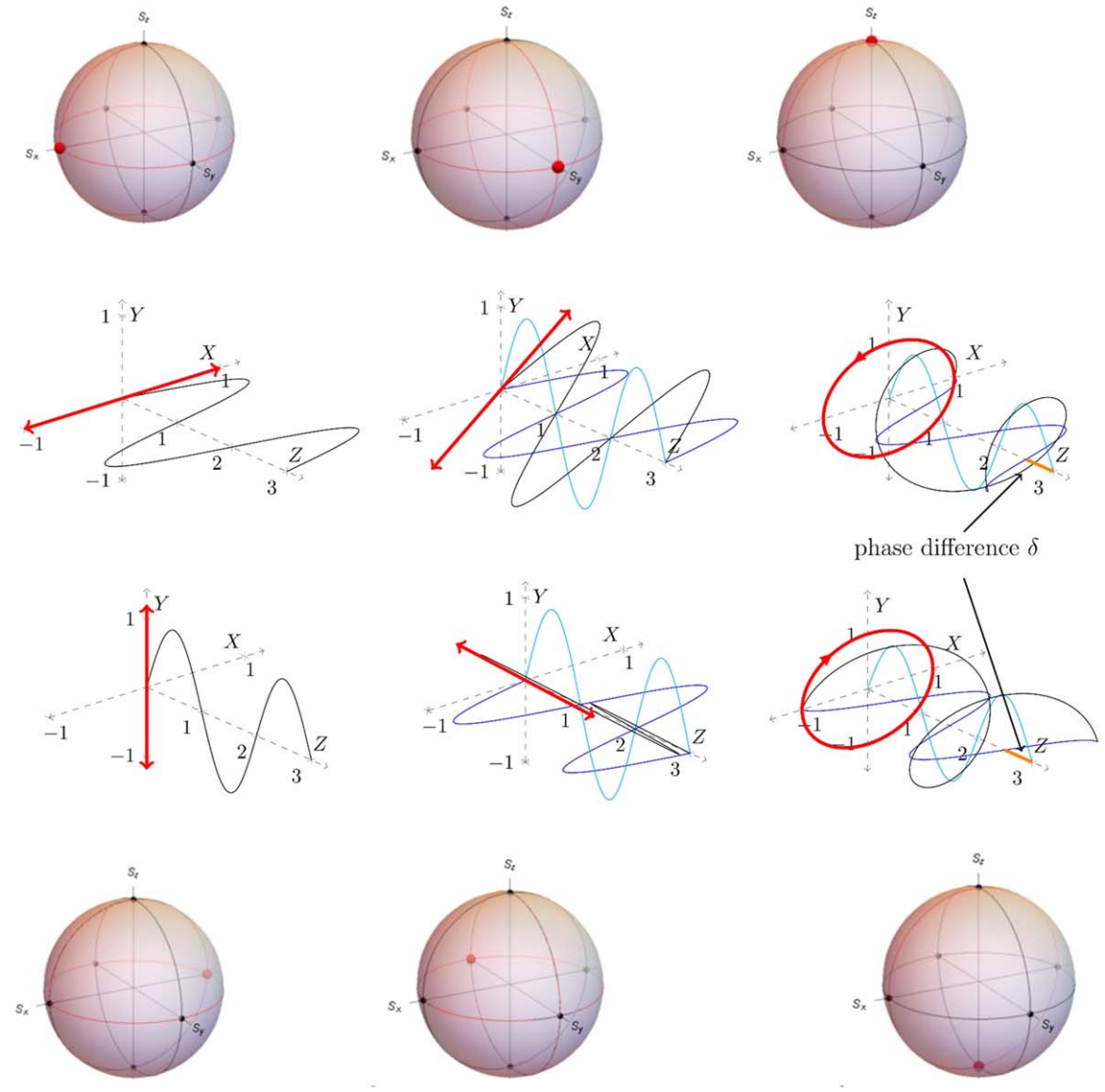

S_1	S_2	S_3
+1	+1	+1
linear horizontal	linear +45°	right circular
-1	-1	-1
linear vertical	linear -45°	left circular

Fig. 2. Schematic representation of the states of polarization with exclusive contributions of S_1 (left), S_2 (middle) and S_3 (right) with a positive sign (top) and a negative sign (bottom). The orthogonal electric field components E_x (blue line) and E_y (cyan line) together with the phase difference (orange stroke), as well as the projection of the resulting electric field radiation(black line) on the xy plane (red) are visible. Corresponding Poincaré spheres are presented for each state. Reproduced and modified from Ref. 39 with permission of Asem Elarabi.

the angle-dependent intensity measured should resemble the shape of a peanut {Fig. 5(b)[left]}, where β is the rotation angle of the WGP relative to the reference direction. For elliptical polarization, the central area of the peanut shape widens {Fig. 5(b)[middle]}. In the context of CP, a minimal to zero change in intensity will be detected at any angle, causing the polarization pattern to appear as a circle {Fig. 5(b)[right]}. From these measurements, the polarization ellipse can be estimated as the tangent to the polarization pattern, thereby providing the AR and the tilt angle. By fitting the recorded intensity using a sine function, the AR in dB can be determined by the following:

$$\mathrm{AR} = 20\log\frac{I_{\max}}{I_{\min}} \tag{14}$$

where $I_{\max}$ and $I_{\min}$ are the maximum and minimum intensities, respectively. It is to be noted that polarization with an AR of less than 3 dB can be regarded as CP.[87)]

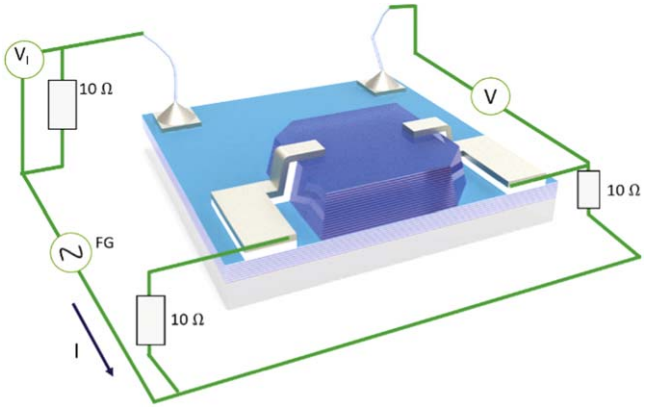

Fig. 3. Block diagram of the electrical setup. Reproduced from Ref. 39 with permission of Asem Elarabi.

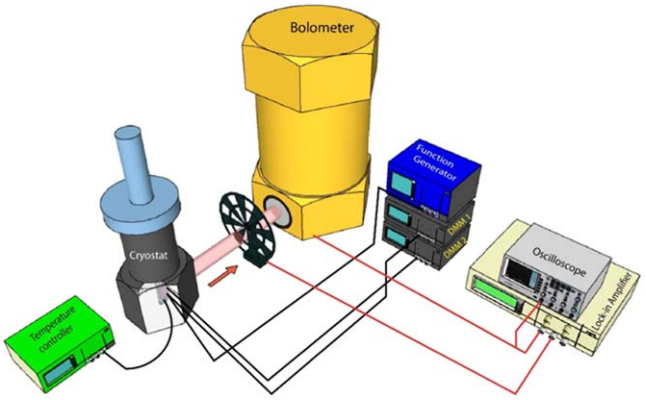

Fig. 4. Sketch for the measurement setup used. Reproduced from Ref. 39 with permission of Asem Elarabi.

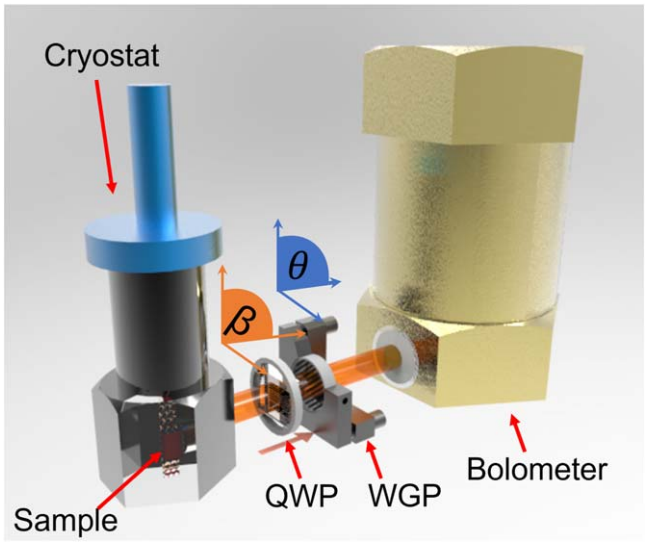

Fig. 6. Sketch of the SPPs measurement setup. Reproduced from Ref. 39 with permission of Asem Elarabi.

4.2.2. Stokes polarimetry with a WGP and a quarter-wave plate. The precise determination of SPPs through Stokes polarimetry is crucial for a comprehensive understanding of the polarization state. Various techniques have been developed to measure these parameters. One conventional method employs a rotating polarizer and a quarter-wave plate (QWP), while another uses a fixed polarizer with a rotating QWP.[80,82,88,89]

The intensity of EM waves passing through a QWP and WGP can be expressed by:[82,90]

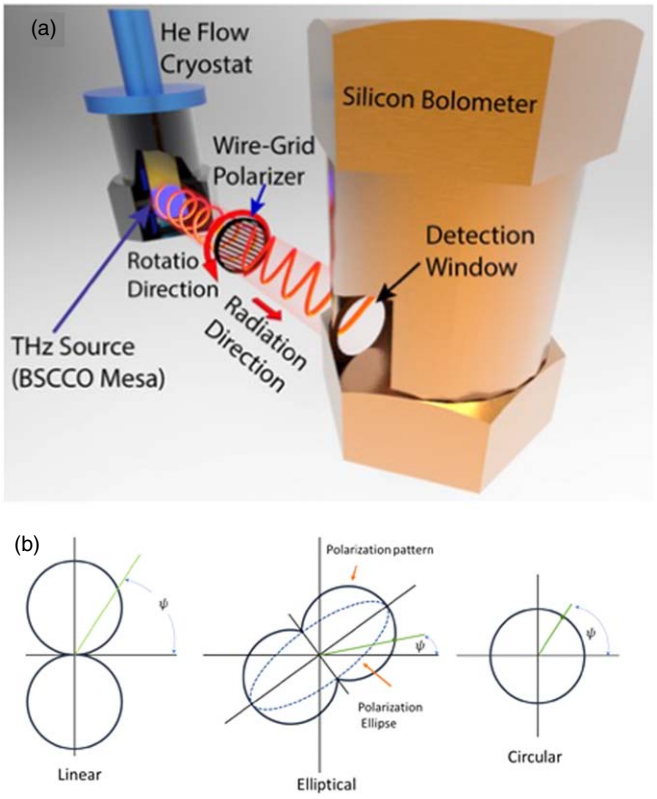

Fig. 5. (a) Sketch of the polarization (AR) measurement setup used. Reproduced from Ref. 40 with permission of Americal Physical Society. (b) Polarization patterns, The dashed curve represents the polarization ellipse. Reproduced from Ref. 39 with permission of Asem Elarabi.

$$I(\theta, \phi) = \frac{1}{2}(S_0 + S_1 \cos 2\theta + S_2 \cos\phi \sin 2\theta + S_3 \sin\phi \cos 2\theta), \quad (15)$$

Where θ is the angle between the transmission axis of the polarizer and the vertical axis, ϕ is the phase retardation ($\phi_{QWP} = \pi/2$). In this method, the parameters can be acquired by measuring four intensities, in terms of ϕ and θ, as follows:

$$I(\theta = 0, \phi = 0) = \frac{1}{2}[S_0 + S_1], \quad (16)$$

$$I\left(\theta = \frac{\pi}{4}, \phi = 0\right) = \frac{1}{2}[S_0 + S_2], \quad (17)$$

$$I\left(\theta = \frac{\pi}{2}, \phi = 0\right) = \frac{1}{2}[S_0 - S_1], \quad (18)$$

$$I\left(\theta = \frac{\pi}{4}, \phi = \frac{\pi}{2}\right) = \frac{1}{2}[S_0 + S_3]. \quad (19)$$

Upon solving for S_0, S_1, S_2, S_3 we can determine the Stokes parameters as follows:

$$S_0 = I(\theta = 0, \phi = 0) + I\left(\theta = \frac{\pi}{2}, \phi = 0\right), \quad (20)$$

$$S_1 = I(\theta = 0, \phi = 0) - I\left(\theta = \frac{\pi}{2}, \phi = 0\right), \quad (21)$$

$$S_2 = 2\, I\left(\theta = \frac{\pi}{4}, \phi = 0\right) - I(\theta = 0, \phi = 0) - I\left(\theta = \frac{\pi}{2}, \phi = 0\right), \quad (22)$$

$$S_3 = 2\, I\left(\theta = \frac{\pi}{4}, \phi = \frac{\pi}{2}\right) - I(\theta = 0, \phi = 0) - I\left(\theta = \frac{\pi}{2}, \phi = 0\right). \quad (23)$$

This conventional technique has certain limitations. It requires measurements with and without QWP in the beam path ($\phi = 0$), which may not be practical for realistic measurements within a nitrogen-purged box and could result in variable total intensity. Moreover, the accuracy may be compromised as only four intensity points are measured. An improved method, adopted in some of our experiments, provides multiple benefits, such as automation and stable intensity. This enhanced technique involves a rotating QWP and a fixed WGP, is illustrated in Fig. 6 and detailed in Refs. 82, 88, 90.

In this improved method, Muller matrices offer a simple and effective means to describe the output state ($\boldsymbol{S}_{out}$) of EM waves passing through ($\boldsymbol{S}_{in}$) an optical element:

$$\boldsymbol{S}_{out} = \overline{\overline{M}}\ \boldsymbol{S}_{in}. \quad (24)$$

The Stokes vectors of the EM wave out of the QWP and fixed WGP using the Muller formalism are expressed by:[82)]

$$\boldsymbol{S}' = \overline{\overline{M_{WGP}}}\ \overline{\overline{M_{QWP}(\beta)}}\ \boldsymbol{S}, \quad (25)$$

where β is the angle between the transmission axis of the QWP and the vertical axis. By solving the matrices, we can find the outcome of $S_0'(\beta)$, which is also known as the total beam intensity, as follows:

$$I(\beta) = S_0'(\beta) = \frac{1}{2}(S_0 + S_1 \cos^2(2\beta) + S_2 \cos(2\beta)\sin(2\beta) + S_3 \sin(2\beta)). \quad (26)$$

This equation can be used to find the Stokes parameters through a multiparameter fitting for the detected intensity.[82,88)] This can be accomplished either during measurements with data acquisition software, or post-measurements using fitting tools.

The DOP is calculated by Eq. (13) The QWP used in our experiment is not conventional (typically made of transparent materials like quartz). Instead, it employs parallel, punctured metallic plates to create a phase delay between the horizontal and vertical components of the passing electric field [Fig. 7 [91,92)]]. This type of QWP benefits from a wide bandwidth and an adjustable target frequency. However, some asymmetry in its transmittance properties were found during testing.

5. Polarizations of rectangular mesas

5.1. Long rectangular mesas

The first JPE was demonstrated on a long rectangular mesa with a high aspect ratio, measuring 300 μm on the long side and 60–100 μm on the short side.[9)] It was pointed out that the emitted EM wave was polarized in the direction of the c-axis of the IJJ stacking. This conclusion was drawn based on the transmission intensity ratio of the oscillating EM wave when passed through a parallel plate filter.

Here we first discuss the consistency of AR measurements using only WGP and SPP measurements with the addition of QWP for radiation from long rectangular mesas. We then compare polarizations between mesas on the same single crystal with very close superconducting properties, and then compare polarizations between mesas on different crystals to discuss the effects of superconducting properties and device geometry on the modifications.

Figures 8(a), 8(b) show the WGP angular (θ) dependence of the detected intensity of mesa B1 at a bias voltage of 1.05 V and the QWP angular (β) dependence of the SPP measurement system, respectively. It should be noted that the device names presented in this manuscript are identical to those of the original papers if they are published. When comparing the ARs obtained listed in Table I, the deviation is about 10 %, indicating a close match. On the other hand, the difference with respect to the specified variable range of 180 degrees is still about 10 %, although the orientation angle Ψ seems to show a relatively large difference. Next, we compare with the polarization in mesa B2 as shown in Figs. 8(c), 8(d). Bias voltages for B1 and B2 are fixed to the conditions that maximize the radiation intensity. The data obtained from both the AR measurement and the SPP measurement agree very well; although the AR measurement of B2 shows a fairly large AR, the AR is greatly affected by the intensity at the node, so it is difficult to say that this is an essential difference in radiation characteristics due to the ambiguity in the origin of the intensity. From the above, it can be seen that the mesas on the same crystal radiate with almost identical polarization characteristics. On the other hand, the polarization of mesa B1 on another crystal is shown in Figs. 8(e), 8(f).

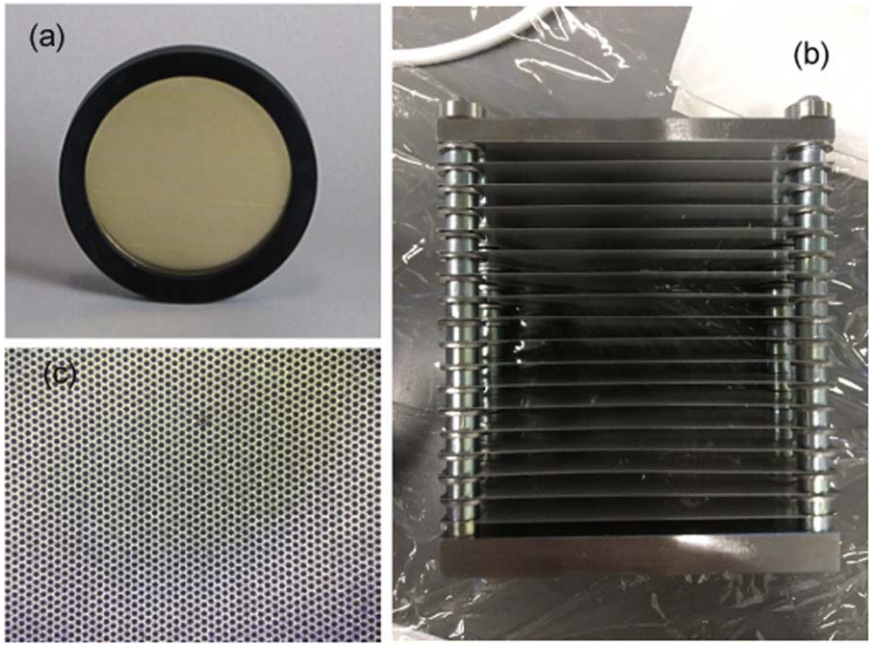

Fig. 7. (a) Photo of the WGP. (b) Photo of QWP. (c) Photo of the plate perforations. Reproduced from Ref. 39 with permission of Asem Elarabi.

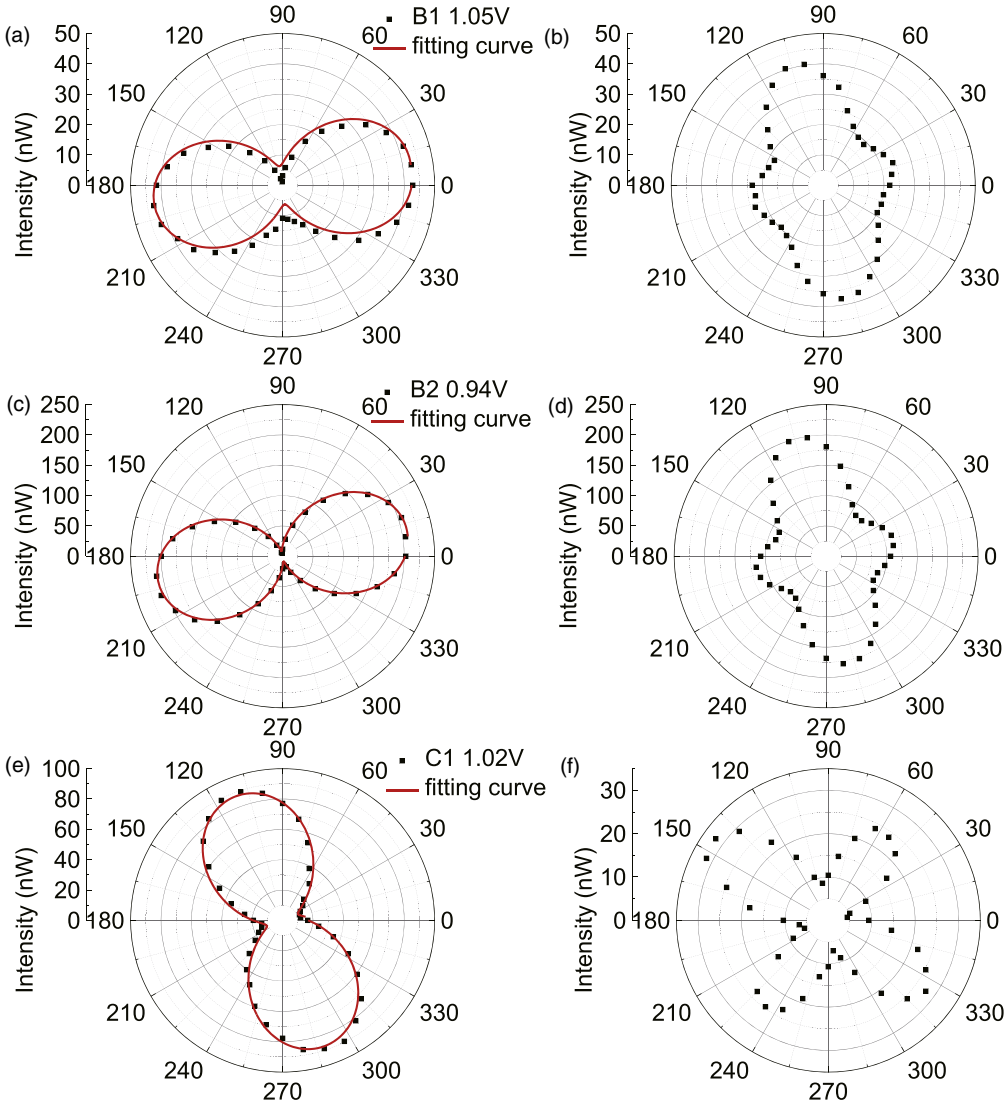

Fig. 8. Polar plots of AR (a), (c), (e) and SPP (b), (d), (f) measurements in mesas B1 (a), (b), B2 (c,d), and C1 (e), (f). Measured data are plotted as black symbols and fitted curves are drawn in red. Partially reproduced from Ref. 46 with permission of Americal Physical Society.

Table I. Summary of obtained polarization parameters by AR (upper rows) and SPP (lower rows) measurements. Here, normalized SPPs $\tilde{S}_i = S_i/S_0 (i = 1, 2, 3)$ are listed.

Mesa	B1	B2	C1	B1‖B2
AR (dB)	8.26	13.6	8.99	5.85
Ψ (deg)	10.7	11.8	−69.3	−3.22
$\tilde{S}_1$	0.298	0.395	−0.60	0.48
$\tilde{S}_2$	0.384	0.478	−0.60	0.01
$\tilde{S}_3$	−0.142	−0.179	−0.13	−0.15
DOP	0.50	0.65	0.86	0.50
AR (dB)	8.35	8.50	11.3	8.06
Ψ (deg)	25.6	25.2	−67.7	0.51

Next, we discuss the device structure and polarization. Polarization measurements of mesas B1 and B2 show that the major axis of polarization, i.e. the major axis of the radiated electric field, is close to the short side direction of the mesa structure. This can be interpreted as the current flowing on the device surface in the short-edge direction being the main source of radiation, which can be explained by the existing standing waves in the short-edge direction alone. However, the results of C1 suggest that the major component originates from the current flowing in the long-sided direction of the mesa. In this case, it implies excitation of Josephson plasma standing waves with finite wavenumber in the y-direction. In both cases, the principal axis of the polarization ellipse is tilted more than 20 degrees from the x- or y-axis, indicating that the oscillating current has components in the x and y directions. Although not with any accuracy that can be considered significant, the observation of the tilted polarization ellipse, including the fact that it is observed, requires a correction to the discussion of the radiation frequency assuming a resonance mode, which has been done in previous studies. The numerical calculations of the radiated electric field are important for a deeper understanding of these phenomena. In the next section, we discuss polarization measurements and numerical calculations to reproduce them for a rectangular mesa of low aspect ratio.

5.2. Short rectangular or square mesas

A wide range of continuous frequency tuning has been reported for rectangular mesas with low aspect ratio (sometimes disk-shaped) with near-square planar geometry since the early stages of research.[35,43] However, identifying resonance modes has proven challenging, leading to extensive discussions regarding the physics of inter-mode transitions. Conversely, in the research on radiation devices from whisker crystals,[44] which advanced due to the simplicity of device fabrication, radiation was obtained from mesa structures with relatively low aspect ratios. However, the distinct chemical composition of whisker crystals means that known values of the refractive index cannot be used, rendering the estimation of the mode challenging. To address this, we compared the radiated EM field calculations with polarization measurements using CST Studio Suite, a three-dimensional EM field simulation software.

Figure 9(a) shows the AR measurement and polarization ellipse for sample 1 of Ref. 45. To reproduce this polarization ellipse, a model is built consisting of a PEC antenna patch and a dielectric with a relative permittivity of $\epsilon_r = 26$. Here, the feeding point of the terahertz current was taken near the corner of the patch. Figure 9(c) shows the polarization ellipse for each probe set up in the calculated space. The polarization observed in the experiment can be considered to be averaged over space. At 729 GHz, near the antenna's resonant frequency (730 GHz), the polarization has a very large AR and is slightly tilted from horizontal. As we move away from the resonant frequency, we see a bulge in the polarization ellipse, and the AR becomes smaller while Ψ becomes larger. It can also be clearly seen that the AR varies with the location of the probe. Spatially averaged results show that 735 GHz best reproduces the experiment. This means that to identify the spatial distribution of polarization is the key information to estimate the standing wave mode, and thus we propose this as a new research method.

6. Polarization of synchronously driven mesas

In the past, attempts have been made to increase the radiation intensity of JPEs by synchronizing the oscillations across multiple mesa devices, aiming to achieve a higher output power compared to operating them individually.[93] The pinnacle of these efforts is marked by a recorded radiation output of 0.6 mW when three mesas were biased simultaneously.[24] This increment in output is hypothesized to stem from the coherent radiation of each mesa. However, no experiments have conclusively demonstrated phase synchronization between the mesas: only a nonlinear enhancement in radiation intensity and a retraction of the radiation frequency have been observed.

Drawing from the insights on polarization measurements delineated in the previous section, we propose a novel approach to analyze the phenomenon of mutual synchronization. By measuring the polarization of EM waves emitted from multiple mesas, whether biased singly or simultaneously, we aim to dive deeper into the underlying mechanics of this synchronization.

6.1. Two mesas synchronization

Figure 10 presents the results when mesas B1 and B2, described in Sect. 5.1 are connected in parallel and biased. The electric field radiated when the mesa is individually biased is expressed as $\boldsymbol{E}_{B1}$ and $\boldsymbol{E}_{B2}$, while the electric field in the parallel bias configuration, denoted $\boldsymbol{E}_{B1\|B2}$ is expressed as a linear coupling with single bias radiation as the basis. In other words, the complex numbers α and β given by

$$\boldsymbol{E}_{B1\|B2} = \alpha \boldsymbol{E}_{B1} + \beta \boldsymbol{E}_{B2}, \tag{27}$$

facilitating a mathematical description of the two-mesas interaction. SPPs for the parallel connection of B1 and B2 are also shown in Table I. The derived values from Table I are $|\beta/\alpha| = 0.98$ and $\arg(\beta/\alpha) = 68.7$ degrees. To evaluate the validity of the coefficients obtained, we compared the phase difference of the coupled standing waves estimated from $\arg(\beta/\alpha)$ and the distance between the mesas. As a result, a phase difference dependent on the distance between the mesas was found by comparing the individual bias and the parallel connection bias.[46] Furthermore, the analysis of the coupling coefficients for another combination of mesa devices B and E, both in parallel and in series connection, at multiple frequencies of synchronous oscillation with a specific basis, showed a systematic change in the declination with the synchronous frequency.[47] The results also show that the difficulty of synchronization changes between parallel

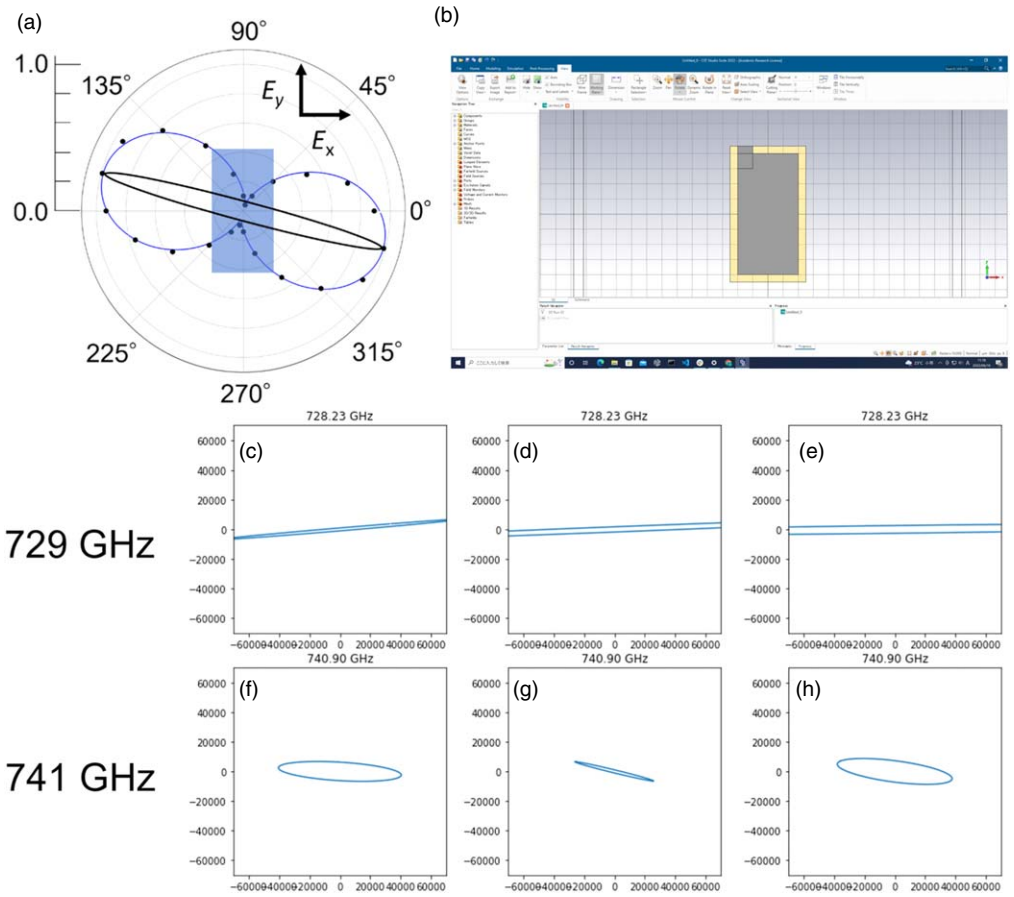

Fig. 9. (a) AR measurement in whisker samples. (b) Calculated anttena model shown by a screenshot of CST studio suite. (c)–(h) Simulated polarization ellipses at 729 and 741 GHz. Virtual probes located at the center (c), (f), right (d), (g), and top (e), (h) with the view shown in (b).

and series connections due to the margin of synchronization conditions and differences in individual radiation characteristics.

The proposed analysis methodology for synchronous radiation phenomena, when applied to relatively diverse mesa structures, promises a pathway towards controlling synchronous oscillation across numerous diverse mesa devices. This progression is anticipated to lead to the development of superconducting devices with enhanced radiation intensity and diversified characteristics, paving the way for real-world applications like ultra-high-speed communication devices.

6.2. Three mesas synchronization

Figure 10(a) shows the result of radiation with mesas B, C, and E connected in parallel.[47] The maximum radiation strength is slightly weaker than the sum of the maximum radiation strengths of the two mesas, but significantly higher than any of the two mesas in parallel [Fig. 10(b)]. The radiation spectrum at voltages close to the maximum intensity [Fig. 10(c)] is unimodal, indicating that the three mesas oscillate synchronously. The relation between the radiation frequency and the average mesa voltage is shown in Fig. 10(d). The Stokes polarization measurements of the BCE parallel connection are shown in [Fig. 10(e)], and the estimated Stokes parameters of the BCE parallel connection are detailed in Table II. Here, adjustments have been made for the intensity reduction due to the tilt of the polarization analyzer. The values to be obtained are the linear combination coefficients α, β, and γ. These coefficients use the oscillating electric field in a BCE stand-alone operation as the basis to reproduce the Stokes parameters in BCE parallel connection by their linear combination.

7. Circularly polarized radiation

Circularly polarized terahertz waves are useful for intermobile communications and in circular dichroism spectroscopy to identify chemical substances. Circularly polarized EM waves have been conventionally obtained in the microwave region by supplying high-frequency current to a specially designed patch antenna and in the optical region by inserting a QWP. In this experiment, we applied the patch antenna concept to demonstrate a monolithic circularly polarized terahertz source using a superconductor.

7.1. TES and notched cylindrical mesas

Figure 11(a) shows the JPE mesa device S1 that radiates circularly polarized terahertz waves with the highest DOCP of 99.7%. The transmission intensity dependence on the linear polarizer's angle is shown in the polar coordinate plot [Fig. 11(b)]. Although the DOCP is strongly dependent on the applied bias voltage or current, it appears relatively stable near the bias voltage that provides the maximum DOCP. The maximum DOCP of the device, or the minimum AR_{min}, is related to the ratio of the length of the truncated edge a_1 to the remaining edge length a_2.

Figure 11(a) illustrates the relationship between the AR and the radiation frequency for a disk mesa device C2, with parts of the outer edges truncated. This behavior is thought to be attributed to the trapezoidal cross section of the mesa

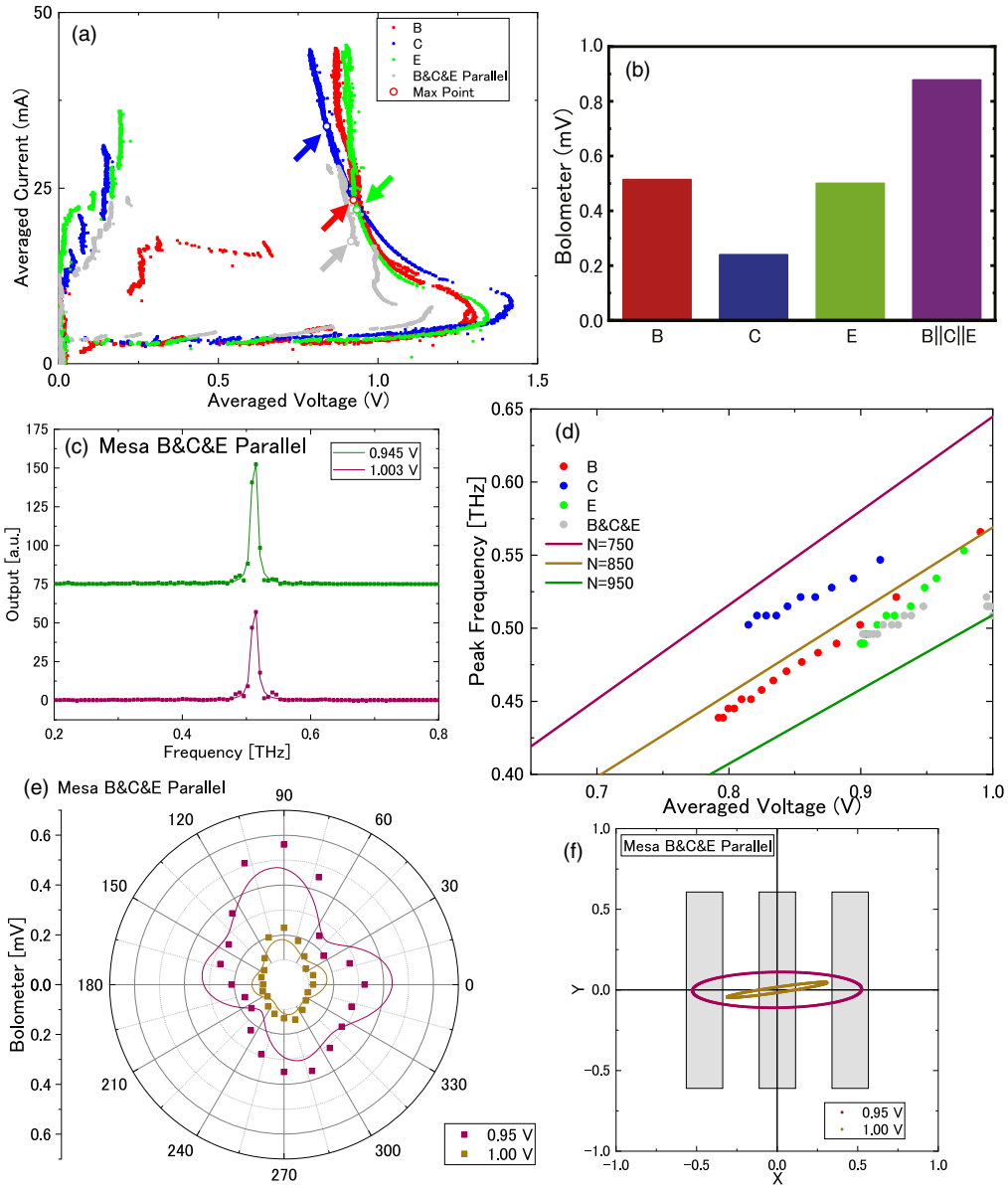

Fig. 10. (a) Current-voltage characteristics of mesa B (red), C (blue), E (green), and all of them connected in parallel (gray). Maximum radiation points were found in open circles for respective colors. The current for the gray plot is divided by three. (b) Comparison of maximum radiation intensities. (c) Fourier transform spectra when mesas B, C, and E are biased in parallel. (d) Radiation frequencies versus applied voltages. (e) Polar plot of SPP measurements for two voltage values of the BCE parallel connection. Asymmetric loss of QWP[47] is considered for the fitting curves. (f) Polarization ellipse for fitting curves in (e).

Table II. Summary of obtained polarization parameters of three mesas radiation. $\tilde{S}_i (i = 1, 2, 3)$ denotes a normalized Stokes parameters, as shown in Table I. Data in mesas B, C and E are selected to be as close to the bias condition of the parallel operation as possible.

Mesa	B	C	E	B&C&E	
Bias voltage (V)	0.94	0.92	0.94	0.95	1.00
S_0	0.99	0.34	0.56	0.31	0.14
$\tilde{S}_1$	0.43	0.94	0.59	0.92	0.89
$\tilde{S}_2$	0.62	−0.048	0.22	0.19	0.45
$\tilde{S}_3$	−0.66	-0.35	0.78	−0.33	−0.037
DOP	0.79	0.98	0.77	0.61	0.40
AR (dB)	4.26	7.47	3.22	7.64	17.3
Ψ (deg)	27.6	−1.48	10.3	5.7	13.3

structure, which induces an entrainment effect between Josephson junctions with differing natural frequencies.

AR measurements were carried out on four truncated-edge mesas and two notched cylindrical mesas. The results are summarized in Table III. Chirality is defined as the position of the perturbed part relative to the current-applying electrode as viewed from the device center. For sample S1 shown in Fig. 11(a), the chirality is right, and the opposite is left. High degrees of CP less than AR = 1 dB are achieved for elements of both chiralities, with the truncated-edge mesa exhibiting the closest approximation to CP around $a_2/a_1 \approx 4$. We also find that a larger thickness t yields higher maximum radiation intensities, which is consistent with the known fact that the intensity is roughly proportional to the square of the stack number.

7.2. Helicity switching

Circularly polarized radiation arises from the resolution of the degeneracy between RHCP and LHCP, which initially exist in a state of linear polarization. Resolution of this degeneracy is facilitated by two primary factors: the chirality of the perturbed region and the position of current injection within the device. These factors influence the local critical current, leading to a decrease in its value.

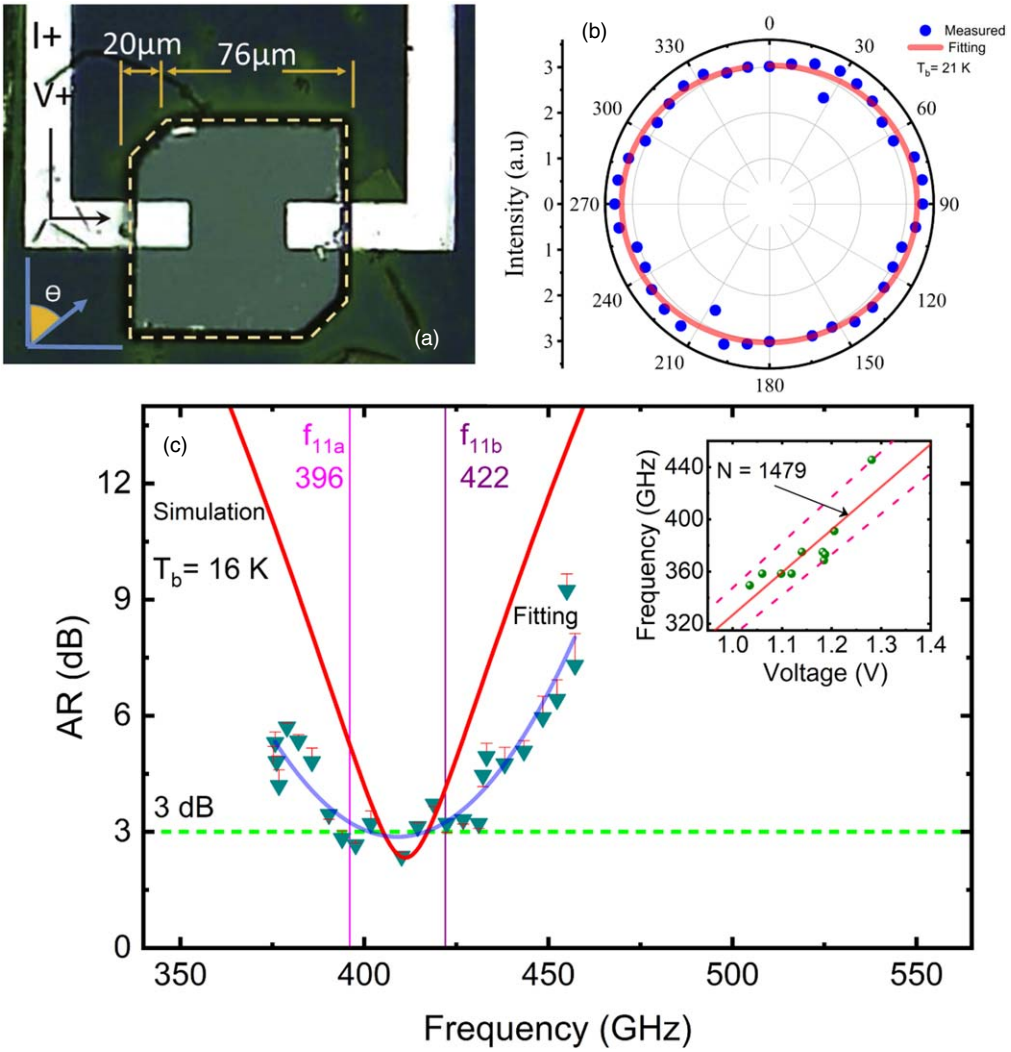

Fig. 11. (a) TES mesa device S1 for CP. The white areas represent electrodes for bias application and measurement. Reproduced from Ref. 40 with permission of Americal Physical Society. (b) Plot in polar coordinates showing the variation of transmission intensity with the polarizer angle under conditions of optimal CP. Reproduced from Ref. 40 with permission of Americal Physical Society. (c) Radiation frequency dependence of the AR in a disk mesa with trimmed cylindrical mesas. The plots marked with inverted triangle symbols represent experimental data, while the red curves are numerical results based on the patch antenna model. The interpolated plots depict the measured radiation frequency dependence on bias voltage. Reproduced from Ref. 42 with permission of AIP Publishing.

Table III. Summary of geometrical and polarization characteristics of CP mesas. a_1 and a_2 are truncated and untruncated length of the truncated-edge squares. r_1 is the depth of the notch and r_2 is the rudius of whole disk in the notched disks. S and ΔS are areas of unperturbed and perturbed parts. t is the thickness of the mesa. T_b and T_c are measured bath temperature and the superconducting transition temperature. P_{max} and AR_{min} are measured maximum intensity and minimum AR.

	S1	S2	S3	S4	C1	C2
Chirality	Right	Right	Left	Left	Left	Left
a_1, r_1 (μm)	16	20	13	18	6	11.2
a_2, r_2 (μm)	70	76	69	68	42	46
a_2/a_1, r_2/r_1	4.38	3.8	5.3	3.77	5.3	4.1
$\Delta S/S$ (%)	3.46	4.34	2.51	4.38	3.46	3.37
t (μm)	2.25	1.9	2.4	2.4	1.9	2.3
T_b (K)	21	22	40	21	30	16
T_c (K)	84	83	82	84	78	85
P_{max} (nW)	176.5	23.5	123.5	88.3	15.3	70
AR_{min} (dB)	0.2	0.49	4.6	0.67	0.8	2.4

The reduction in the local critical current is instrumental in achieving the desired helicity switch, allowing for the transition between RHCP and LHCP. To demonstrate this helicity switch within a single device, we fabricated a device capable of altering its chirality. By doing so, we can switch the helicity of the radiated EM wave. We further investigated the radiated terahertz wave emanating from the device to observe the effects of helicity switching.

SPP measurement results of the device shown in Fig. 12(a) when current is injected from electrode L are presented in Fig. 12(b). The fitting line to obtain the Stokes parameter is shown as a solid line. The radiation frequency was found to be 564 GHz and the normalized Stokes vector was $\tilde{\boldsymbol{S}} = (0.073, -0.867, 0.491)$. This means that left-handed elliptical polarization was detected. When a bias is applied to electrode R, the helicity switch is successfully achieved at

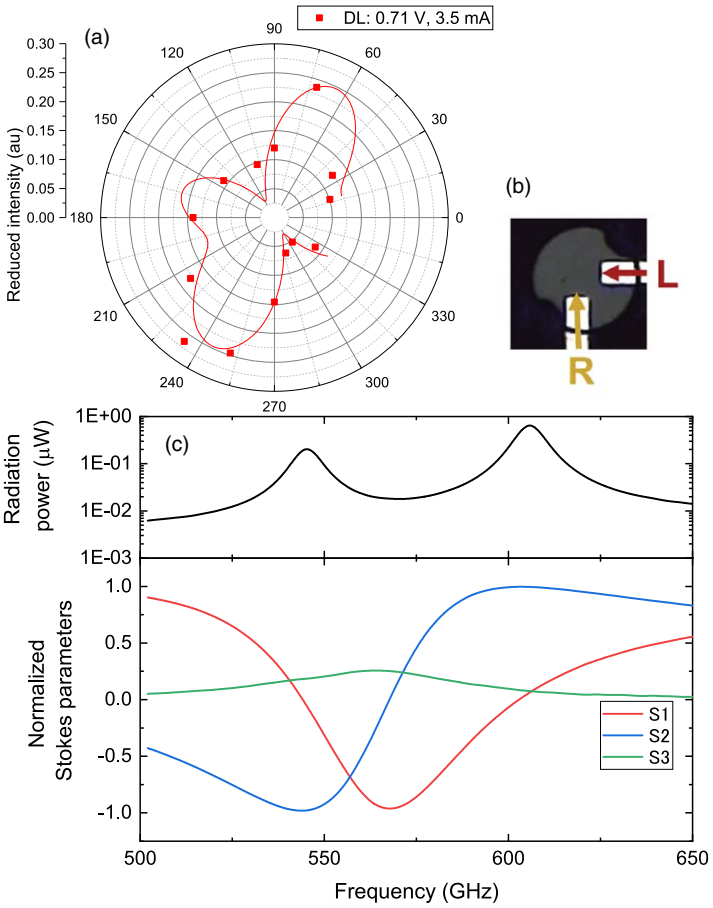

Fig. 12. (a) Polar plot of SPP measurement when current is applied to the electrode "L" of the device shown in (b), which is referred to as DL. (c) Expected radiation power (upper) and SPPs (lower) as functions of frequency obtained by solving sine-Gordon equation in a model corresponding to DL.

570 GHz with $\tilde{S} = (0.197, -0.867, -0.456)$, which means that the right-handed elliptical polarization is detected. Figure 12(c) shows the radiation frequency dependence of the radiation intensity and Stokes parameters calculated using the sine-Gordon equation for an idealized mesa geometry as shown in the inset. The calculated $\tilde{S}_3 > 0$ obtained around the measured radiation frequency of 564 GHz is consistent with the experimental results. However, the values of $\tilde{S}_1$ and $\tilde{S}_2$ are quite different from the experiment. This may be due to the fact that not only the actual planar shape of the mesa differs, especially with respect to the angle of the cut, but also that the mesa has a larger cross-sectional area toward the bottom near the substrate, which requires a 3D model for accurate description. A paper is currently being written on the results of detailed experimental data analysis and numerical simulation refinement.

8. Summary

This manuscript highlights recent progress in exploring polarized terahertz radiations generated by IJJ emitters. The relization of CP is led by two distinct designs: a TES mesa structure and a notched cylindrical structure, demonstrating the utility of antenna theory and EM simulations in achieving the desired polarization. The methodology, based on the excitation of IJJs within a mesa cavity, effectively addresses the insertion loss challenges associated with external polarimetric modulators in the terahertz frequency range. A brief discussion of polarization characterization methods is provided, with examinations that include long and short rectangular mesas, whisker devices, and multiple synchronously driven mesas. Although the helicity of the emitted EM wave is a crucial feature of circularly polarized waves, its comprehensive understanding remains not fully understood despite recent strides. The ongoing research in circularly polarized terahertz radiation is poised to drive advancements in practical realms like mobile communications and circular dichroism spectroscopy, highlighting the practical significance of the findings.

Acknowledgments

This work was supported by the Japan Society for the Promotion of Science (JSPS) KAKENHI (Grant Nos. 23K17747, 20H02606, 15KK0204), JSPS—Centre national de la recherche scientifique (CNRS) Bilateral Program (Grant No. 120 192 908), and the Murata Science foundation.

ORCID iDs

Asem Elarabi https://orcid.org/0000-0001-7541-3756
Ryota Kobayashi https://orcid.org/0009-0003-7915-3666
Yoshihiko Takano https://orcid.org/0000-0002-1541-6928
Manabu Tsujimoto https://orcid.org/0000-0003-4296-5137
Itsuhiro Kakeya https://orcid.org/0000-0003-4999-2111

1) M. Tonouchi, Nat. Photonics **1**, 97 (2007).
2) B. Ferguson and X.-C. Zhang, Nat. Mater. **1**, 26 (2002).
3) S. S. Dhillon et al., J. Phys. D. Appl. Phys. **50**, 043001 (2017).
4) J. F. Federici, B. Schulkin, F. Huang, D. Gary, R. Barat, F. Oliveira, and D. Zimdars, Semicond Sci. Technol. **20**, S266 (2005).
5) K. Kawase, Y. Ogawa, Y. Watanabe, and H. Inoue, Opt. Express **11**, 2549 (2003).

6) X. C. Zhang, A. Shkurinov, and Y. Zhang, Nat. Photonics **11**, 16 (2017).
7) B. S. Williams, Nat. Photonics **1**, 517 (2007).
8) M. Asada and S. Suzuki, J. Infrared Millim. Terahertz Waves. **37**, 1185 (2016).
9) L. Ozyuzer et al., Science **318**, 1291 (2007).
10) U. Welp, K. Kadowaki, and R. Kleiner, Nat. Photonics **7**, 702 (2013).
11) I. Kakeya and H. Wang, Supercond. Sci. Technol. **29**, 073001 (2016).
12) T. Kashiwagi et al., Supercond. Sci. Technol. **30**, 074008 (2017).
13) R. Kleiner and H. Wang, J. Appl. Phys. **126**, 171101 (2019).
14) K. Delfanazari, R. A. Klemm, H. J. Joyce, D. A. Ritchie, and K. Kadowaki, Proc. IEEE **108**, 721 (2020).
15) I. Kakeya, IEICE Trans. Electron. **E106.C**, 2022SEI0004 (2023).
16) T. Kashiwagi et al., Appl. Phys. Lett. **106**, 092601 (2015).
17) H. Sun et al., Appl. Sci. (Switzerland) **13**, 3469 (2023).
18) K. Kihlstrom et al., Phys. Rev. Appl. **19**, 034055 (2023).
19) L. Y. Hao et al., Phys. Rev. Appl. **3**, 024006 (2015).
20) H. Minami et al., J. Phys.: Condens. Matter **28**, 025701 (2016).
21) H. Sun et al., Phys. Rev. Appl. **10**, 024041 (2018).
22) T. Imai, T. Kashiwagi, S. Nakagawa, M. Nakayama, J. Kim, G. Kuwano, M. Tsujimoto, H. Minami, and K. Kadowaki, Jpn. J. Appl. Phys. **60**, 126501 (2021).
23) T. Kashiwagi et al., IEICE Trans. Electron. **E106.C**, 281 (2023).
24) T. M. Benseman et al., Appl. Phys. Lett. **103**, 022602 (2013).
25) D. Tilley, Phys. Lett. A **33**, 205 (1970).
26) K. Wiesenfeld, S. P. Benz, and P. A. A. Booi, J. Appl. Phys. **76**, 3835 (1994).
27) R. Kleiner, F. Steinmeyer, G. Kunkel, and P. Müller, Phys. Rev. Lett. **68**, 2394 (1992).
28) R. Kleiner and P. Müller, Phys. Rev. B **49**, 1327 (1994).
29) K. Schlenga et al., Phys. Rev. B **57**, 14518 (1998).
30) M. Tachiki, T. Koyama, and S. Takahashi, Phys. Rev. B **50**, 7065 (1994).
31) T. Koyama and M. Tachiki, Solid State Commun. **96**, 367 (1995).
32) M. Tachiki, M. Iizuka, K. Minami, S. Tejima, and H. Nakamura, Phys. Rev. B **71**, 134515 (2005).
33) S.-Z. Lin and X. Hu, Phys. Rev. B **82**, 020504 (2010).
34) R. A. Klemm and K. Kadowaki, J. Phys.: Condens. Matter **22**, 375701 (2010).
35) M. Tsujimoto, K. Yamaki, K. Deguchi, T. Yamamoto, T. Kashiwagi, H. Minami, M. Tachiki, K. Kadowaki, and R. A. Klemm, Phys. Rev. Lett. **105**, 037005 (2010).
36) H. Asai and S. Kawabata, Appl. Phys. Lett. **110**, 132601 (2017).
37) H. Asai and S. Kawabata, IEEE Trans. Appl. Supercond. **26**, 1800804 (2016).
38) C. Balanis, *Antenna Theory: Analysis and Design* (Wiley, New York, 2015).
39) A. Elarabi, "Polarization behavior of high-Tc superconducting terahertz emitters," PhD Thesis Kyoto University (2018).
40) A. Elarabi, Y. Yoshioka, M. Tsujimoto, and I. Kakeya, Phys. Rev. Appl. **8**, 064034 (2017).
41) A. Elarabi, Y. Yoshioka, M. Tsujimoto, Y. Nakagawa, and I. Kakeya, Phys. Procedia **81**, 133 (2016).
42) A. Elarabi, Y. Yoshioka, M. Tsujimoto, and I. Kakeya, Appl. Phys. Lett. **113**, 052601 (2018).
43) M. Tsujimoto et al., Phys. Rev. Lett. **108**, 107006 (2012).
44) Y. Saito et al., Appl. Phys. Express **14** (2021).
45) Y. Saito, I. Kakeya, and Y. Takano, Appl. Phys. Lett. **121**, 212601 (2022).
46) M. Tsujimoto et al., Phys. Rev. Appl. **13**, 051001 (2020).
47) R. Kobayashi, K. Hayama, S. Fujita, M. Tsujimoto, and I. Kakeya, Phys. Rev. Appl. **17**, 054043 (2022).
48) K. Maeda, S. Fujita, A. Elarabi, M. Tsujimoto, and I. Kakeya, 2019 XLIV Int. Conf. Infrared, Millimeter, Terahertz Waves (IEEE), 2019, p. 1.
49) M. Sato et al., Nat. Photonics **7**, 724 (2013).
50) R. Takeda, N. Kida, M. Sotome, Y. Matsui, and H. Okamoto, Phys. Rev. A **89**, 033832 (2014).
51) N. Amer, W. C. Hurlbut, B. J. Norton, Y.-S. S. Lee, and T. B. Norris, Appl. Phys. Lett. **87**, 1 (2005).
52) J. Dai, N. Karpowicz, and X.-C. Zhang, Phys. Rev. Lett. **103**, 023001 (2009).
53) Y. You, T. Oh, and K. Kim, Opt. Lett. **38**, 1034 (2013).
54) R. Shimano, H. Nishimura, and T. Sato, Jpn. J. Appl. Phys. **44**, L676 (2005).
55) Y. Chen et al., Appl. Phys. Lett. **93**, 3 (2008).
56) S.-Y. Wang, W. Liu, and W. Geyi, Appl. Phys. B **124**, 126 (2018).
57) C. Zhang et al., IEEE Trans. Antennas Propag. **65**, 385 (2017).
58) B. Yan, M. Jansen, and C. Felser, Nat. Phys. **9**, 709 (2013).
59) B. Lin, J.-L. Wu, X.-Y. Da, W. Li, and J.-J. Ma, Appl. Phys. A **123**, 43 (2017).
60) H. Chen et al., Appl. Phys. A **122**, 463 (2016).
61) G. Zhou et al., Sci. Rep. **6**, 38925 (2016).
62) Z. Li, W. Liu, H. Cheng, S. Chen, and J. Tian, Sci. Rep. **5**, 18106 (2016).
63) K. Saito, T. Tanabe, and Y. Oyama, Opt. Express **20**, 26082 (2012).
64) F. Li et al., Appl. Phys. B **124**, 28 (2018).
65) X. Ma et al., Adv. Opt. Mater. **2**, 945 (2014).
66) Y. Tamayama, K. Yasui, T. Nakanishi, and M. Kitano, Appl. Phys. Lett. **105**, 021110 (2014).
67) L. Wu et al., Appl. Phys. A **116**, 643 (2014).
68) X. Jiang et al., Phys. Rev. Lett. **94**, 056601 (2005).
69) M. Holub, J. Shin, D. Saha, and P. Bhattacharya, Phys. Rev. Lett. **98**, 146603 (2007).
70) P. Rauter et al., Proc. Natl. Acad. Sci. **111**, E5623 (2014).
71) N. Yu et al., Appl. Phys. Lett. **151101**, 1 (2009).
72) G. Liang et al., ACS Photonics **4**, 517 (2017).
73) L. Xu et al., Optica **4**, 468 (2017).
74) M. Tsujimoto et al., Supercond. Sci. Technol. **28**, 105015 (2015).
75) R. A. Klemm et al., IOP Conf. Ser.: Mater. Sci. Eng. **279**, 012017 (2017).
76) G. Kuwano et al., J. Appl. Phys. **129** (2021).
77) M. Tsujimoto et al., Opt. Express **29**, 16980 (2021).
78) H. Minami, Y. Ono, Y. Saito, T. Yuhara, R. Kikuchi, T. Kashiwagi, M. Tsujimoto, and K. Kadowaki, Proc. XXIX Int. Conf. Low Temp. Phys. (Journal of the Physical Society of Japan), 2023, 10.7566/JPSCP.38.011047.
79) W. A. Shurcliff, *Polarized Light: Production and Use* (Harvard University Press, Cambridge, MA, 1962).
80) E. Collett, "Polarized light: fundamentals and applications," *Optical Engineering* (Marcel Dekker, New York, 1993).
81) C. Brosseau, *Fundamentals of Polarized Light: A Statistical Optics Approach* (Wiley, New York, 1998).
82) A. Molitor, "Investigations on Stokes polarization parameters of Vertical-Cavity Surface- Emitting Lasers : spatially, spectrally and time-resolved," PhD Thesis Technische Universitat Darmstadt (2015).
83) G. G. Stokes, "On the composition and resolution of streams of polarized light from different sources," *in Mathematical and Physical Papers* (Cambridge Univ. Press, Cambridge, U.K, 2009) 1st ed., Vol. 3, p. 233.
84) D. H. Martin and E. Puplett, Infrared Phys. **10**, 105 (1970).
85) R. L. Henry and D. B. Tanner, Infrared Phys. **9**, 59 (1969).
86) O. Ferhanoglu, H. R. Seren, S. Luettjohann, and H. Urey, Opt. Express **17**, 21289 (2009).
87) S. Gao, Q. Luo, and F. Zhu, *Circularly Polarized Antennas* (Wiley, Chichester, UK, 2014), 10.1002/9781118790526.
88) H. G. Berry, G. Gabrielse, and A. E. Livingston, Appl. Opt. **16**, 3200 (1977).
89) B. Schaefer, E. Collett, R. Smyth, D. Barrett, and B. Fraher, Am. J. Phys. **75**, 163 (2007).
90) B. Schaefer, E. Collett, R. Smyth, D. Barrett, and B. Fraher, Am. J. Phys. **75**, 163 (2007).
91) N. Mukai et al., Int. Conf. on Infrared, Millimeter, and Terahertz Waves, IRMMW-THz, 2014, Vol. 39, p. 146.
92) M. Nagai et al., Opt. Express **23**, 4641 (2015).
93) N. Orita, H. Minami, T. Koike, T. Yamamoto, and K. Kadowaki, Phys. C: Supercond. Appl. **470**, S786 (2010).